J. Fluid Mech. (2006), *vol.* 555, *pp.* 409–437.
doi:10.1017/S002211200600927X Printed in the United Kingdom

Experimental studies of vortices shed from cylinders with a step-change in diameter

By W. DUNN AND S. TAVOULARIS

Department of Mechanical Engineering, University of Ottawa, Ottawa, Canada K1N 6N5

(Received 15 January 2005 and in revised form 4 November 2005)

The interactions of vortices shed from two coaxially joined cylinders with a diameter ratio of 0.51 have been studied in a water channel, at Reynolds numbers, based on the large cylinder diameter, between 63 and 1100. Spectral and wavelet analyses of streamwise velocity measurements have identified the formation of three distinct spanwise vortex-shedding cells away from the far ends of the two cylinders, including a low-frequency cell, which appeared in a cyclic manner near the step and behind the large cylinder. Analysis of flow-visualization images has identified two distinct types of vortex connection at cell boundaries: some vortices in a cell of lower frequency connected across the boundary to counterparts in the cell of higher frequency, while others formed a half-loop to connect to a vortex shed from the opposite side of the cylinder in the same cell. Additional cross-boundary vortex connections balanced the total vortex strengths. The interactions of two types of streamwise vortices, identified as edge vortices and junction vortices, with spanwise vortices have also been documented.

1. Introduction

Vortex shedding from circular cylinders and other elongated objects has been a topic of intense study for a long time (Bénard 1908; Kármán 1911; Zdravkovich 1997, 2003; Williamson 1996). At first glance, it might be expected that a cylinder of uniform diameter in uniform flow would shed, at a regular rate, two-dimensional vortices, parallel to its axis. In reality, two-dimensional vortices have been observed only for specific conditions, and only within a narrow Reynolds-number range. Far more common are configurations with three-dimensional vortex patterns. These include uniform cylinders in non-uniform flow streams, cylinders with non-uniform cross-sections, and cylinders with relatively low aspect ratios or attached to solid walls. In such cases, vortices are shed in cellular patterns along the cylinder span, with a distinct frequency within each cell, and an abrupt frequency change across the boundaries of adjacent cells.

Williamson (1989) studied vortices at the boundaries to cells near the ends of uniform cylinders fitted with endplates. He observed that the frequency of vortices in the end cell was lower than that in the main cell and that some end-cell vortices connected continuously across the cell boundary with counterparts in the main cell, while others connected to more than one vortex in the main cell. This phenomenon of multiple vortex connections has been described in the literature as vortex splitting and, alternatively, as vortex dislocation. Cellular vortex shedding has also been observed behind uniform cylinders in shear flows (Mair & Stansby 1975), tapered cylinders in uniform flows (Gaster 1969), and finite cylinders that ended abruptly in the flow (Ayoub & Karamcheti 1982).

Oblique vortex shedding, cellular vortex shedding and vortex splitting are common in three-dimensional wake flows. These processes can be best studied under experimental conditions designed to generate non-uniform vortex shedding in a controlled manner. In a detailed visual study, Williamson (1992) examined vortex dislocations by attaching a thin ring of larger diameter at the midspan of a cylinder. The ring shed vortices at a frequency slightly lower than that along the rest of the cylinder and vortex dislocations formed periodically at the beat frequency, defined as the difference between the frequencies in adjacent cells.

Three-dimensionality in vortex shedding has also been studied using step-cylinders, formed by joining coaxially two cylinders with different diameters, d and $D > d$. Velocity spectra in the wakes of large-aspect-ratio step-cylinders with diameter ratios in the range $0.5 < d/D < 0.65$, and excluding the end regions, have identified three vortex-shedding frequencies. Besides the two main frequencies in the wakes of the large and small cylinders, a third frequency, lower than both, has been found to occur in a cell behind the large cylinder adjacent to the step (Lewis & Gharib 1992; Norberg 1992). At a Reynolds number of 3×10^3, the span of this cell was approximately $9D$, and decreased with increasing Reynolds number and d/D. A boundary between the low-frequency cell and the main cell behind the large cylinder could be seen to form and disappear periodically. While present, this boundary was inclined and, when viewed at a fixed streamwise location, it moved gradually away from the step over several vortex-shedding cycles, following which it suddenly disappeared. The cell thus appeared to grow in span over some cycles and then collapse abruptly. Lewis & Gharib (1992) called this cell the 'modulated zone', because the velocity variation within this cell was modulated by the main frequency behind the large cylinder, especially close to the cell boundary. Modulation of velocity signals, which has been associated with the formation of vortex dislocations, has also been observed near cell boundaries in other configurations (Gaster 1969; Ayoub & Karamcheti 1982; Williamson 1989).

A number of additional studies have examined various aspects of vortex shedding from step-cylinders. Yagita, Kojima & Matsuzaki (1984) and Ko & Chan (1984) found that vortex shedding behind the small cylinder was relatively unaffected by the discontinuity in diameter. Ko, Leung & Au (1982) suggested that the flat side of the step might isolate the vortices shed by the small cylinder from those shed by the large cylinder, much as an endplate isolates the ends of a cylinder from the walls of the test section. Using hot-wire anemometry, Chua, Liu & Chan (1998) found two spectral peaks in the wake of the large cylinder close to the step, corresponding to the two main vortex-shedding frequencies from the two cylinders. The region in which both peaks occurred moved in the spanwise direction away from the step and toward the large cylinder with increasing downstream distance, in agreement with the observations of Lewis & Gharib (1992).

A fundamental aspect of vortex shedding from step-cylinders is the interaction between vortices with a significant frequency difference across the step. Because the large cylinder sheds vortices at a lower rate than the small cylinder does, such connections cannot be one-to-one. It has been observed that some vortices shed from the large cylinder are nearly in-phase with counterparts shed from the small cylinder and connect to them across the cell boundary, while others are shed out-of-phase, in which case the large-cylinder vortex has no direct counterpart among the small-cylinder vortices, and vortex splitting occurs. The frequency of vortex-splitting occurrences is approximately equal to the difference in the two shedding frequencies. Different authors have represented vortex splitting as either two high-frequency vortices connecting to a single low-frequency vortex (Yagita *et al.* 1984; Norberg 1992), or

Configuration		Diameter (mm)	Length (mm)	AR	d/D
1	d	3.43	318	92.7	0.52
	D	6.60	318	48.2	0.52
2	d	6.60	318	48.2	0.51
	D	13.0	318	24.5	0.51

TABLE 1. Cylinder dimensions.

as two high-frequency vortices shed from opposite sides of the small cylinder, joining together through half-loops (Lewis & Gharib 1992; Valles, Andersson & Jenssen 2002). In addition to the mainly spanwise shed vortices, Ko & Chan (1984) suggested that streamwise vortices might also be generated by the sharp edges of the step.

Despite the effort that has been made toward the description of cellular vortex-shedding patterns near cross-sectional discontinuities, understanding of this topic remains incomplete. The step-cylinder remains an attractive test configuration, because it isolates a single cross-sectional discontinuity from other geometric complications, such as free ends, additional adjacent discontinuities, gradual cross-sectional changes and the like. Although atmospheric boundary layers and other practical flow environments have non-uniform, and often unsteady, velocity fields, it is preferable to examine first the simpler case of a uniform steady free stream before addressing more complex cases. Understanding of vortex generation and interactions in this idealized configuration may help the understanding of more complex patterns in bluff-body wakes encountered in engineering applications. The objective of the present work is to further document experimentally the flow around a circular cylinder with a step-change in diameter, with emphasis on the vortex characteristics and interactions in the step region. The experiments consist of high-resolution visualization of the flow around models placed in a low-speed water channel, and instantaneous velocity measurements using laser-Doppler velocimetry (LDV). A combination of qualitative and quantitative analyses was employed to provide a thorough explanation of the observed complex patterns.

2. Experimental facilities and procedures

2.1. *Water channel, models and test conditions*

All experiments were conducted in a closed-circuit water channel, with a volume of approximately $16\,\mathrm{m}^3$ of water. The test section was 4 m long, with a cross-section 0.50 m wide and 0.75 m high. It was enclosed on three sides by 9.5 mm thick glass walls, while its top surface was kept free. All instruments and models were placed in the test section from above. Motorized carriages mounted above, below and along one side of the test section allow mounting and traversing of models and instruments in and around the water channel.

All cylinders were made of stainless steel, and covered by lead foil of thickness 0.13 mm, which was used for flow-visualization purposes. The dimensions of the cylinders, including the lead foil thickness, are shown in table 1. The water height in the test section was $h = 690\,\mathrm{mm}$, and the flow speed was uniform and varied in the range $6.5\,\mathrm{mm\,s^{-1}} < U_\infty < 96\,\mathrm{mm\,s^{-1}}$ for different tests. This speed was determined by spatially averaging measurements taken over the central 50 % of the cross-sectional area of the test section. The Reynolds number based on the large cylinder diameter, $Re_D = DU_\infty/\nu$, was in the range $62 < Re_D < 1230$. The Reynolds-number range for

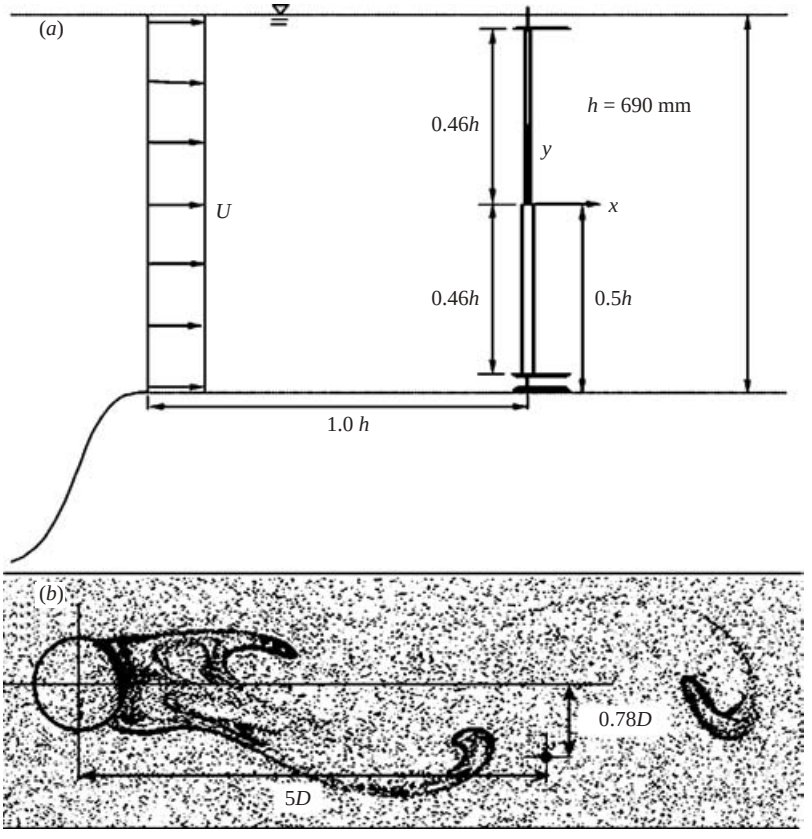

FIGURE 1. (*a*) Cylinder layout. The cylinder is shown in the upright configuration, but was also tested inverted. (*b*) LDV measurement location superimposed on a flow-visualization image, using electrolytic precipitation illuminated by a laser light sheet at $Re_D = 80$.

the small cylinder, $Re_d = dU_\infty/\nu$, was $32 < Re_d < 627$. The cylinders were secured to the bottom of the test section and to a support above the water surface. All figures have been oriented such that the large cylinder was located below the small cylinder (figure 1). The large-diameter section was placed above the small cylinder during some tests, in order to identify possible dependence of vortex shedding on the cylinder orientation, mounting process or channel flow imperfections. In order to reduce end effects, two endplates were used, placed 25 mm below the water surface and above the bottom of the test section. The endplates were transparent circular disks, 3 mm thick and 100 mm in diameter, with a rim that was chamfered 60° to a sharp edge on the side facing the central section. The centres of the endplates were placed at approximately 25 mm downstream of the cylinder axes, in an effort to improve the definition of the cell boundaries (Mair & Stansby 1975).

2.2. *Flow-visualization procedures*

Visualization of the shed vortices was achieved using electrolytic precipitation of lead and by the production of hydrogen bubbles. Electrolytic precipitation of the lead foil that covered the cylinder surfaces produced a colloidal suspension of nearly spherical lead oxide tracer particles with diameters of the order of 1 μm (Taneda, Honji & Tatsuno 1979). The particles were white, providing excellent contrast against a dark background. Sodium carbonate was added to the water as required to maintain a

pH close to 7.0, and a voltage difference between 40 V and 100 V, depending on the Reynolds number, was applied between the lead anode and a graphite rod placed downstream, which served as a cathode. The visibility of the precipitate was inadequate at speeds higher than 50 mm s^{-1}, owing to rapid diffusion. After some use, the surface of the cylinder was covered by a residue of the chemical reaction, which blocked further reaction. This deposit was removed with medium-grain sandpaper, followed by fine-grain sanding to reduce the surface roughness.

Hydrogen bubbles were produced by electrolysis of water around a thin wire cathode, 0.04 mm in diameter, made of Alloy C (Jelliff). The wire was mounted in a frame that could be adjusted from 10 to 300 mm in length, and could be oriented at any angle to the flow. All electrically conducting surfaces other than the active wire were coated with silicon caulking for safety purposes, and to avoid the production of stray bubbles. The circuit was completed by a graphite rod anode, which was placed in the water nearby, but far enough away not to interfere with the flow being studied.

Illumination of the tracers was mainly produced using a 750 W projector lamp (Buhl Optical, with a DDB bulb), which provided uniform light across the entire beam. Additional high-power spotlights were used to reduce shadows. Laser light sheet illumination was produced by passing the beam of a 5 W argon-ion laser through a Powell lens, which was connected to the laser by a fibre optic cable with a capacity of 1 W. Images were recorded with a digital video camera (Sony DCR-VX1000) at a rate of 30 frames s^{-1}.

2.3. *Laser-Doppler velocimetry*

A two-component laser-Doppler velocimetry system (Dantec), operating in back-scatter mode, was used for velocity measurements. The measurement volume of the streamwise velocity component was $0.078 \times 0.077 \times 0.650\,\mathrm{mm}^3$. The Doppler signals were analysed by a 16 bit burst processor (DANTEC BSA F50), resulting in a velocity resolution of 3.9×10^{-6} m s^{-1}. The flow was seeded with silicon carbide spheres, 1.5 μm in diameter, producing data rates of at least 30 samples s^{-1} for the flow speeds used, which were sufficient for spectral measurements.

Velocity measurements were taken at locations 5 diameters downstream of, and 0.78 diameters off-centre from, the corresponding cylinder axis (figure 1*b*). The cylinder span was traversed at 116 locations in 2 mm to 5 mm increments, and the free-stream speed was monitored 20 diameters upstream of the cylinders before each spanwise set was completed, using a coarse grid of roughly 50 mm increments.

The velocity data obtained from the LDV system were randomly spaced. Because evenly spaced time series are required for spectral and wavelet analyses, the data were resampled at a rate of 25 Hz using the sample-and-hold technique (Adrian & Yao 1987). Data records of 205 s were acquired at each location. Each record was divided into three blocks with an overlap of 25 % and processed by a fast Fourier transform (FFT) algorithm, which computed spectra with a frequency resolution of 0.012 Hz.

2.4. *Wavelet analysis procedure*

Space–time analysis of the measured velocity was achieved with the use of the wavelet transform, based on the Morlet wavelet (Daubechies 1992; Farge 1992; Torrence & Compo 1998). The shape of the Morlet wavelet is determined by modulating a complex sinusoidal function by a Gaussian envelope,

$$\psi(\tau) = \pi^{-1/4} \exp(\mathrm{i}2\pi\gamma\tau) \exp(-\tau^2/2). \tag{1}$$

The wavelet is defined by specifying a dimensionless frequency γ and a dimensionless time τ. The continuous wavelet transform of a continuous function $s(\tau)$ is given

by its convolution with the wavelet,

$$W(a,\tau) = \int \frac{1}{\sqrt{a}} s(\tau')\psi^*\left(\frac{\tau'-\tau}{a}\right) \mathrm{d}\tau', \tag{2}$$

where the asterisk denotes complex conjugate. The normalization factor $a^{-1/2}$ is included so that the energy of the wavelet remains constant as it is scaled by the dimensionless scale a (Jordan, Miksad & Powers 1997). As γ is also scaled in the process, each scale corresponds to a 'local' frequency in the time history at a particular time. When the wavelet transform is applied to a discrete time series with a sampling time Δt, the actual local frequency corresponding to a given scale can be calculated as (Abry 1997; Gordeyev & Thomas 1999)

$$f = \frac{\gamma}{a\Delta t}. \tag{3}$$

The dimensionless frequency of the Morlet wavelet was taken to be $\gamma = 1$ and the local frequencies computed with equation (3) were converted into Strouhal numbers for consistency with the rest of the data.

The amplitude of the wavelet transform computed by equation (2) will be presented in the form of iso-contours, plotted against the actual time and the Strouhal number. The amplitude was normalized by its largest value within each plot, to illustrate the relative significance of phenomena recurring at different frequencies, with larger amplitudes indicated by darker shading. The term 'amplitude peak' will be used to describe the largest amplitudes, similar to the use of the term 'spectral peak' in a power spectrum. Cross-sections of the wavelet map parallel to the Strouhal number axis at a given instant in time may be viewed as 'local' frequency spectra, having peaks at dominant local Strouhal numbers.

2.5. *Measurement uncertainty*

The only flow property that was measured directly was the time-dependent streamwise velocity component, whose uncertainty would propagate into that of all derived parameters. The main source of uncertainty related to the water-channel operation was due to low-frequency surface waves that propagated along the test section, whereas the uncertainty caused by changes in flow speed due to evaporation and by errors in positioning of the cylinders and LDV probe was found to be negligible.

The surface waves had a frequency of about 0.1 Hz, independent of flow speed, and an amplitude of typically about $4\,\mathrm{mm\,s^{-1}}$ for a nominal speed of $101\,\mathrm{mm\,s^{-1}}$. All velocity signals were high-pass filtered to remove the wave frequency before spectral and wavelet analyses were performed; because the frequencies of the spectral peaks were at least one decade higher than the wave frequency, the peaks were not affected by this filtering. Even so, the signals could contain some variability in shedding frequency owing to surface wave-induced periodic fluctuations in flow velocity. This frequency variability cannot be removed and could express itself as a broadening of the spectral peaks. For a nominal speed of $101\,\mathrm{mm\,s^{-1}}$, this would introduce an uncertainty in the determination of frequency of approximately $\pm 2.2\,\%$ for the large cylinder, and $\pm 3.1\,\%$ for the small cylinder. Because most of the spectral peaks were quite sharp, and broadening was observed mostly around the base of the peaks, it may be inferred that the actual frequency uncertainty would be much smaller than the above estimates. Most of the cells showed an abrupt change in frequency at their boundaries. The lower bound for the frequency jump across cell boundaries at the above flow speed was approximately 7 % behind the large cylinder, which is nearly twice the

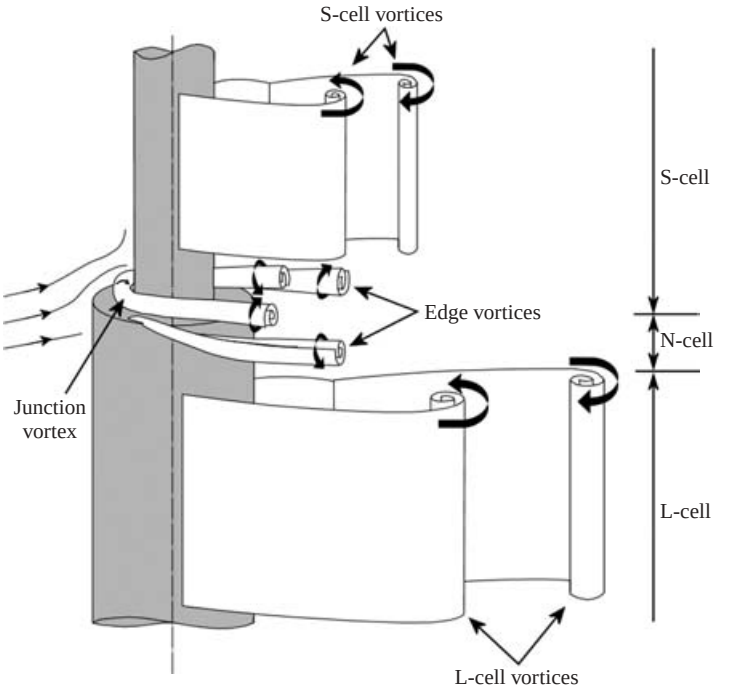

FIGURE 2. Different types of vortices near the step cylinder. Additional vortices are shed in the N-cell, but have not been sketched in consideration of their complexity.

upper bound of the frequency uncertainty. Moreover, the wave-induced fluctuations introduced a random uncertainty, and cannot produce cells of constant frequency along the cylinder span. The uncertainty of Strouhal number was much lower than that of the frequency, because the Strouhal number was normalized by the mean velocity, time-averaged over 205 s, which mostly averaged out the wave effect whose period was only 10 s. The only source of Strouhal number uncertainty was a very small residual effect due to the nonlinearity of the *St–Re* curve.

3. Results and discussion

3.1. *Definitions*

To assist in the description of the observed complex vortical patterns, some specific terminology has been introduced, which is summarized in schematic form in figure 2.

As will be explained in detail in the following sections, two general kinds of vortex were generated by the step cylinder.

(i) Spanwise vortices, which were shed in cells with constant frequency; the two 'main' cells behind the large and small cylinders will be called, respectively, the *L-cell* and the *S-cell*, while a third cell near the step behind only the large cylinder will be called the *N-cell*.

(ii) Streamwise vortices, which were of two kinds: the *junction vortex*, of hairpin shape and wrapped around the base of the small cylinder, and the two *edge vortices*, which rolled up over the sides of the step toward the large cylinder.

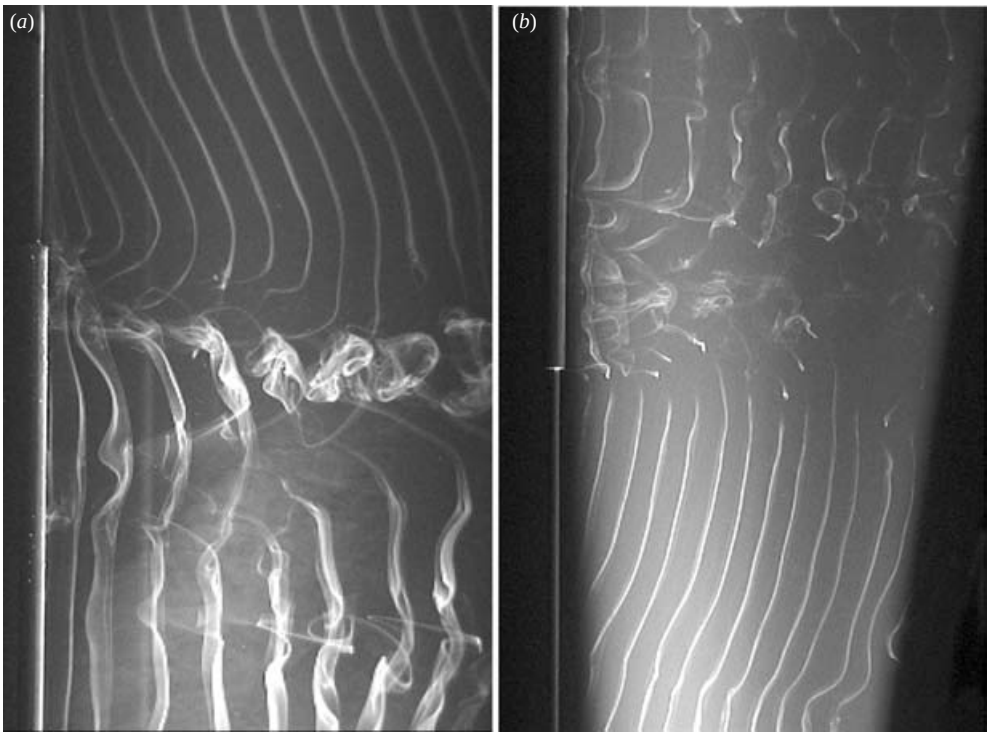

FIGURE 3. Vortex-shedding patterns from the step-cylinder in (*a*) the standard orientation at $Re_D = 152$ and (*b*) the inverted configuration at $Re_D = 168$. The vortices were visualized using the electrolytic precipitation method.

3.2. *Effect of cylinder orientation*

Before presenting the results, it seems advisable to discount the possibility that the observed patterns might be artefacts of the cylinder mounting procedure, or extraneous effects associated with flow imperfections or the water-channel operation. Typical vortex-shedding patterns behind a step-cylinder with a diameter ratio $d/D = 0.51$ are shown in figure 3(*a*) with the cylinder in its standard orientation and in figure 3(*b*) with the cylinder inverted. The same shedding patterns were observed for both orientations, and the vortices maintained consistent inclinations with respect to the cylinder. This supports the assessment that the observed flow features are genuinely associated with the specific geometry of the cylinder, and not due to spurious effects. Any differences between figures 3(*a*) and 3(*b*) are attributed to the non-stationary nature of the observed shedding patterns, which were not repeated precisely, even with the same geometrical set-up and under the same flow and lighting conditions. These include differences in the location of gaps in the vortices, vortex curvature and the apparent thickness of the vortices.

3.3. *Vortex appearance away from the step*

As a consequence of Reynolds-number differences and the presence of the step, the appearance of vortices in the main cell of the small cylinder (S-cell vortices) differed from those in the main cell of the large cylinder (L-cell vortices). An example is shown in figure 3(*a*), in which the Reynolds number was 79 for the small cylinder and 152 for the large cylinder. The S-cell vortices were laminar and mostly parallel

to each other, and remained so, even far downstream from the step. In general, these vortices were uninterrupted along the span of the cylinder up to a few diameters from the step, with only occasional waviness that lasted for short times. In contrast, the L-cell vortices were in transition to a disorganized three-dimensional motion and only nominally parallel to each other. In agreement with observations at comparable Reynolds numbers (Zdravkovich 1997), these vortices were characterized by waviness along their lengths, and streamwise 'fingers', which were visible at various spanwise locations. These fingers formed soon after the vortices detached from the cylinder surface, often appeared to link subsequent vortices far downstream, and eventually decayed or were scrambled by unstable motions and became unrecognizable.

Excluding the spanwise region within a few diameters of the step, both sets of vortices were inclined in the same sense with respect to the axis of the cylinder. Starting at about five diameters away from the step, the S-cell vortices were inclined such that the part closer to the step was always farther downstream than the part away from the step. This implies that the shedding of each vortex started closer to the step region and moved spanwise away from the step. The inclinations of these vortices were reversed close to the step, to levels that varied from one vortex to another. In contrast, shedding of N-cell vortices appears to have started on the far side and moved spanwise toward the step. Observations of long video sequences confirmed that the inclinations of both sets of vortices were systematic and consistent, so that they must be associated with the effects of the step.

A plausible explanation for the S-cell vortex inclination away from the boundary with the N-cell is as follows. The base pressure of the large cylinder is lower than that of the small cylinder, creating a tendency for the small-cylinder wake to spill into the large-cylinder wake. This is apparent in figure 3, which shows that vortices shed from the small cylinder extended spanwise beyond the step level. As fluid separates over the sharp trailing edge of the step, it rolls up into the wake of the large cylinder, generating a form of 'downwash' and possibly triggering the early shedding of an S-cell vortex close to the step. Parts of the same vortex away from the step are shed with some delay, such that the vortex appears to be inclined. The sharp reversal of S-vortex inclination near the boundary with the N-cell can be explained by the fact that the vortex-shedding frequency in the N-cell is much lower than that in the S-cell (see next section; also Lewis & Gharib 1992; Norberg 1992), so that cross-boundary vortex connections retard the shedding of S-cell vortices (Williamson 1989 provides a similar explanation for vortex inclination near the ends of long uniform cylinders). The inclination of the L-cell vortices can be explained by similar reasoning, as the frequency in the N-cell is also lower than that in the L-cell.

Video sequences showed that vortex inclinations varied gradually from one vortex to another, between about 0° and 30° with respect to the cylinder axis. The inclinations of S-cell vortices were more often observed in the higher portion of this range, while those of L-cell vortices were more often in the lower portion.

3.4. *Identification of vortex-shedding cells and their boundaries*

The formation of cells in the vortex-shedding patterns caused by the change in the cylinder diameter was documented by both flow visualization and by velocity spectra measured in the cylinder wake five local diameters downstream. The cell boundary locations were observed to vary with time, a process that cannot be faithfully analysed by single-point measurements. Even so, velocity spectra are useful because they provide time-averaged boundary locations and dominant shedding frequencies, which

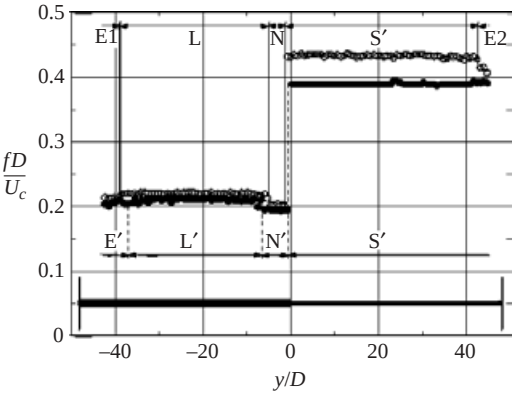

FIGURE 4. Dimensionless frequency of vortices shed from a step-cylinder in uniform flow at $Re_D = 304$ (●) and 627 (○); a sketch of the cylinder and the endplates is provided at the bottom of the figure.

allow comparisons among the different cases as well as with previous studies (e.g. Norberg 1992), which present only time-averaged information.

The frequency at which the highest spectral peak occurred has been plotted against spanwise distance in figure 4 for $Re_D = 304$ and 627, with both frequency and spanwise distance normalized by the large diameter. Consistently with two-dimensional vortex-shedding patterns, a change in vortex-shedding frequency was observed as the diameter changed, defining a cell S (S′ at $Re_D = 627$) behind the small cylinder, and a cell L (L′), with a much lower frequency, behind the large cylinder. In agreement with the observations of Lewis & Gharib (1992) and Norberg (1992), a third cell, N (N′), was detected near the step, behind the large cylinder. The frequency in this cell was lower than those in either S- or L-cells, being approximately 7 % lower than that in the L-cell at both $Re_D = 304$ and 627. Additional cells E1 (E′) and E2 were observed close to the endplates. These are attributed to end effects, and, because of the relatively large aspect ratios of the cylinders, they do not play any role in the vortex development near the step.

The boundary between the N- and S-cells could easily be discerned in flow-visualization images such as figure 3. Downwash from the step caused the N–S cell boundary to be deflected spanwise in the direction of the large cylinder, with the deflection increasing with downstream distance. Similar observations were made by Ko, Chan & Kan (1983) based on pressure spectra. Flow visualization shows that spanwise deflections of the N–S cell boundary extended by several diameters and varied with time, depending on the state of the N-cell. Attempts to quantify this deflection using spectral measurements from figure 4 were inconclusive. Five local diameters downstream, the N–S cell boundary was detected at $y/D = -0.5$ for $Re_D = 304$, and at $y/D = -1.2$ for $Re_D = 627$. Both of these boundary locations are much closer to the step than flow visualization indicated. A possible explanation for this discrepancy is that the LDV measurements were always taken at a fixed distance (0.78 local diameters) from the plane of symmetry, while the instantaneous maximum deflection might have occurred on a different plane.

Oblique views of the cylinders, together with the free stream and other details of the flow, were provided by hydrogen bubbles generated by a wire stretched at different positions in the flow (figure 5). Because the bubbles were lighter than the surrounding water, they tended to concentrate in the inner cores of vortices and in recirculation

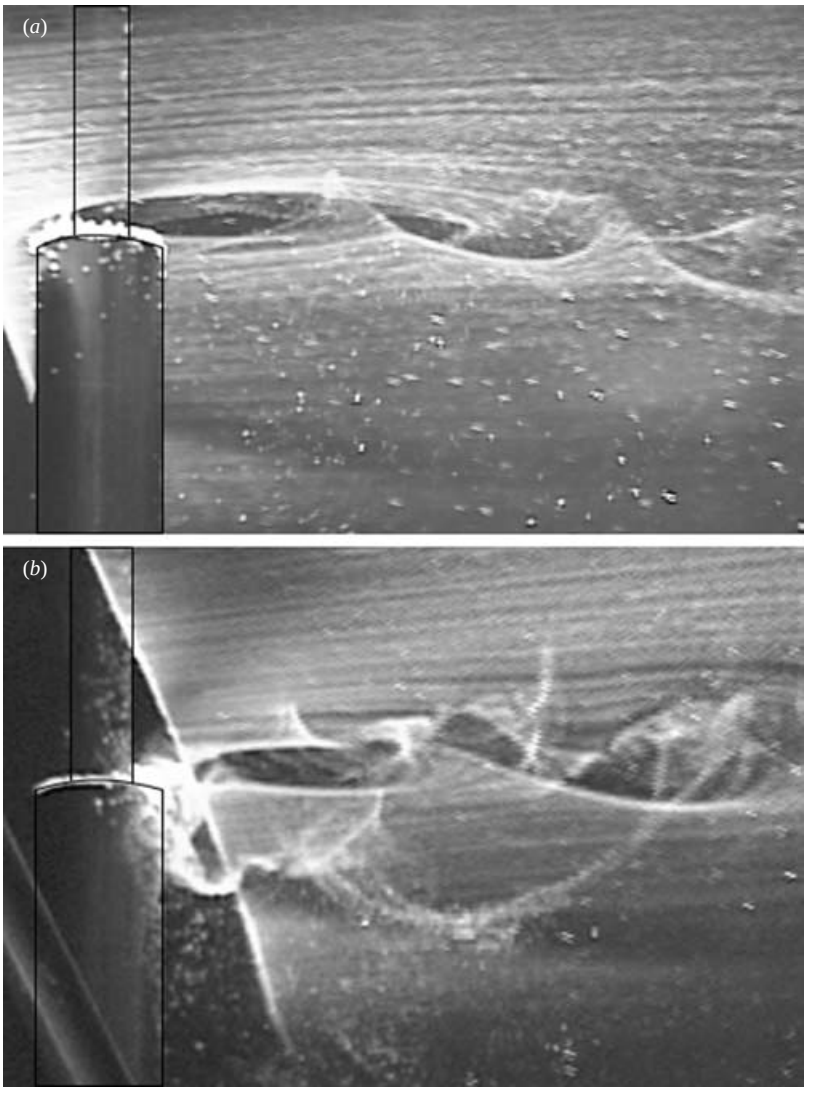

FIGURE 5. Hydrogen bubble visualization of vortex shedding at $Re_D = 298$. (*a*) S-cell vortices, (*b*) S-cell and edge vortices, with downwash visible close to the cylinder.

regions and so they provided clearer views of edge vortices and downwash than electrolytic precipitation particles. These photos were taken off-axis to the cylinders, so they also illustrate the three-dimensionality of vortex interactions. With the wire placed on the plane of the step upstream of the cylinder, only S-cell vortices could be observed (figure 5*a*), because, as seen earlier, the N–S cell boundary was deflected spanwise toward the large cylinder. With the bubble sheet placed downstream of the cylinder and slightly towards the large cylinder (figure 5*b*), a more complex pattern of vortex interactions is visible, including long streamwise filaments that stretched between several consecutively shed vortices.

The boundary between the N- and L-cells was visible in the flow visualizations as a series of gaps in the shedding pattern behind the large cylinder several diameters away from the step (figure 3). Unlike the change in frequency across the S–N cell

boundary, which is large and clearly associated with the change in cylinder diameter, the change in frequency across the N–L cell boundary is relatively small and possibly caused by a more subtle mechanism. At a given downstream location, the N–L cell boundary was not fixed, but drifted spanwise with time, and occasionally disappeared abruptly and could not be seen for several vortex-shedding cycles. Spectra measured in the boundary region identify time-averaged frequencies and cannot be used to locate the instantaneous boundary position. Based on figure 4, the average location of the N–L cell boundary five local diameters downstream of the cylinder axis was at $y/D = -7.3$ at $Re_D = 304$, and at $y/D = -5.2$ at $Re_D = 627$. For comparison, the average boundary location at $Re = 152$, calculated from flow-visualization sequences, was at approximately $y/D = -13$. Thus, both the N–S and the N–L cell boundaries defined from spectra appeared to be closer to the step than flow-visualization indicated.

The cell boundaries shown in figure 4 were determined by locating the spanwise position at which a change in the dominant spectral frequency occurred. However, in agreement with Papangelou's (1992) observations in experiments with tapered cylinders, the peak frequency changed gradually over a spanwise distance, rather than abruptly. This is illustrated by the spanwise variation of spectra shown in figure 6 at $Re_D = 304$. At $y/D = 1.8$, the spectrum consisted of a single peak at $St = 0.390$, corresponding to the vortex-shedding Strouhal number in the S-cell. At $y/D = -0.3$, near the nominal cell boundary, a second peak of lower amplitude appeared at $St = 0.198$, corresponding to the Strouhal number in the N-cell. With increasing distance from the step, the second peak increased in amplitude, became comparable to the dominant peak, and eventually became dominant itself. At the same time, the high-frequency peak decreased continuously and disappeared at around $y/D = -0.6$. These results indicate that the location of the N–S cell boundary was not fixed in either space or time, but fluctuated over a spanwise distance of approximately $\pm 0.25D$ about its nominal position.

Inspection of spectra near the N–L cell boundary (figure 6*d–g*) also showed a gradual changeover from one frequency to another. At $y/D = -3.3$, a single peak occurred at $St = 0.198$. At $y/D = -6.4$, close to the nominal cell boundary, a second peak appeared at $St = 0.209$. On the other side of the boundary, at $y/D = -7.6$, the second peak was higher than the first, while, further away, at $y/D = -9.1$, only the second peak remained. The observed broadness in the peaks is probably the result of continuously changing vortex inclination, which can alter the instantaneous frequency of the streamwise velocity signal (Williamson 1996). Peaks at both frequencies were identifiable in the spectra for at least $2D$ on either side of the cell boundary, and the two frequency peaks had comparable magnitudes for about $1.5D$. In comparison to the N–S cell boundary, the N–L cell boundary occupied a much broader spanwise range, which is consistent with the flow-visualization observations.

Altogether, the N-cell had a cyclic appearance: at its formation, it had a short spanwise length, which continuously grew with time up to a moment when it suddenly disappeared and remained absent for short durations, following which the cycle restarted. In a still image such as figure 3(*a*), the cell appears triangular in shape, with inclined boundaries on either side, and the N–L cell boundary typically having a larger inclination (with respect to the streamwise direction) than the N–S cell boundary. This triangular pattern was convected downstream in the wake of the large cylinder, so that, from a fixed reference point, each cell boundary appeared to change spanwise position with time. The N-cell was characterized by intense mixing, spreading of the vortex cores, and the formation of streamwise disturbances near its

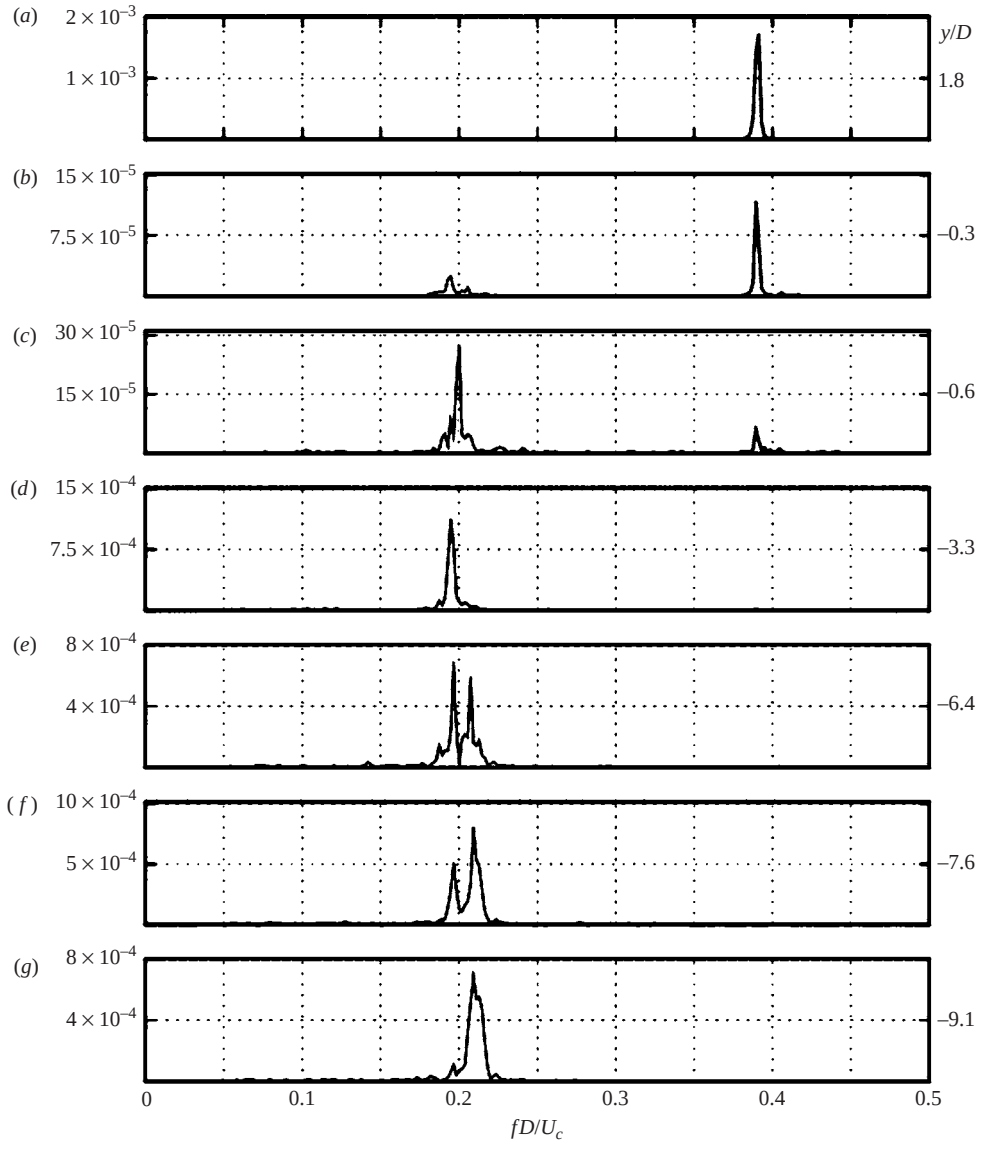

FIGURE 6. Velocity spectra for the step-cylinder at $Re_D = 304$. The large cylinder is located at negative values of y/D.

boundaries. Lewis & Gharib (1992) called this cell the 'modulated zone', because the vortex-shedding frequency was modulated by the average frequency in the adjacent L-cell. They found that the amplitude of the modulation increased as the N–L cell boundary was approached, and that the local frequency near that boundary alternated regularly between the dominant frequencies in the N- and L-cells.

In closing this section, it seems worth revisiting the question of why the N-cell appears. Previous literature on step-cylinders offers little assistance on this matter, as neither Lewis & Gharib (1992) nor Norberg (1992) attempt to explain its formation or the frequency difference between vortices in the N- and L-cells. Nevertheless, low-frequency cells have also been observed near the free ends of uniform cylinders (e.g.

Ayoub & Karamcheti 1982), a configuration which, despite its differences, is relevant to the step cylinder case. Zdravkovich *et al.* (1989) attribute these cells to downwash over the free end, which tends to increase the base pressure in that region; downwash causes the vortex formation length to increase beyond that in the main cell, so that the separated shear layers become wider before rolling up, resulting in a lower shedding frequency. Williamson (1989) also suggests that an increase in base pressure near the ends of long uniform cylinders increases the length of the vortex-formation region, resulting in lower frequencies in the end cells. He was able to eliminate the end cells altogether by manipulating the endplates to reduce the base pressure. A similar explanation seems appropriate for the N-cell formation in step-cylinders. In support of this explanation, figure 5(*b*) shows clearly visible downwash over the step into the wake of the large cylinder. We may speculate that, owing to the smaller base pressure gradients near steps compared to those near free ends, downwash would be weaker in the former case and would further diminish as the cylinder diameter ratio approaches unity. In support of this speculation, Ayoub & Karamcheti (1982) measured a 23 % frequency drop from the main cell to the end cell of a cylinder with one free end, which is much larger than the 7–14 % drop observed in the current study (see §§ 3.4 and 3.5.3). Moreover, Lewis & Gharib (1992) reported that the N-cell disappeared altogether for $d/D > 0.8$.

The cyclical nature of the N-cell is more difficult to account for. Ayoub & Karamcheti (1982) found that the downwash action over a cylinder with a free end was cyclical, even disappearing for short durations. The downwash in the present case was also observed to be cyclical, although the available data are insufficient to establish a direct correspondence between the cycles of downwash and the N-cell occurrence.

3.5. *Vortex connections at cell boundaries*

3.5.1. *Vortex connectivity*

A main concern of this study is to clarify what happens to spanwise vortices at cell boundaries. It is obvious that vortices in one cell cannot connect with counterparts in an adjacent cell on a one-to-one basis, because the numbers of vortices shed into different cells per unit time are different, and the strengths of vortices vary from one cell to the next. For an approximate rationalization of vortex connections using inviscid concepts, consider the following first and second Helmholtz vortex theorems.

(i) The strength of an isolated vortex is constant along its length; consequently, the sense of rotation of an isolated vortex must be consistent along its entire length.

(ii) A vortex cannot terminate in the fluid; it may, however, form a closed loop.

The strength of an isolated vortex is defined as the circulation Γ around a closed path surrounding it. Assuming that Stokes' theorem (also strictly applicable to inviscid flows) is approximately valid for shed vortices, this circulation would be equal to the surface integral of the vorticity contained in the vortex, which should be approximately equal to the surface integral of the vorticity shed from the cylinder's surface into each vortex. In other words, the rate of vorticity production around the cylinder in a regular vortex street should be equal to the product of Γ and the vortex-shedding frequency f. Previous experimental and theoretical studies using uniform cylinders have correlated the rate of vorticity production with the free-stream velocity U as

$$\Gamma f = \Lambda U^2, \tag{4}$$

where $\Lambda \approx 0.4$ for the range $62 < Re < 200$ (Berger & Wille 1972; Zdravkovich 1997). Assuming that this also applies to vortices shed from step-cylinders in uniform flow,

the strengths of vortices within each cell would be inversely proportional to their shedding frequencies, which vary from one cell to another. As a result, vortices should be stronger in the L-cell compared to those in the S-cell. In view of the limited spanwise extent of the N-cell and its cyclical appearance, as well as considering that there is vorticity production by flow over the step, the relevance of equation (4) to N-cell vortices is questionable. Nevertheless, the small difference in frequency between the N- and L-cell vortices implies that differences in the strengths of vortices in these cells would probably also be small.

At a cell boundary, vortices may connect to other vortices either within the same cell or in an adjacent cell. Two vortices on opposite sides of the boundary having the same senses of rotation may connect directly to each other to form a single vortex, but this would leave an excess circulation (strength) in one of them, which would require a connection to a third vortex. Adjacent vortices in the same cell would have equal strengths, but opposite senses of rotation. They may connect to each other through a half-loop branch to form a hairpin-like vortex, or may have more complex connections involving additional vortices. Besides these two possibilities there are many others, as each vortex may connect to several other vortices, both spanwise and streamwise. According to Williamson (1989), the process of vortex splitting and reconnecting would be such that the sum of the strengths of all parts of vortices that contribute to a connection would be preserved across the connection. Thus, if a single vortex is split into two vortices, the strength of the single one would be equal to the sum of the strengths of the two others.

3.5.2. *Vortex connections at the N–S cell boundary*

Figure 7(*a*) shows a typical sequence of different vortices and their connections near the N–S cell boundary. The vortex-shedding frequencies in the S- and N-cells, calculated from the video sequence (not from spectra), were $f_S = 1.0$ and $f_N = 0.53$, respectively. For rough purposes, we may assume that the N-cell vortex strength can be predicted by equation (4), as applied to the L-cell. This implies that the strength of N-cell vortices should be roughly 1.9 times higher than the strength of S-cell vortices. Vortex connections varied in a cyclical manner, and are not always easy to discern in still images, being much more evident in the video sequence. In order to aid in their visualization, the main vortex connections that were identified in figure 7(*a*) have been sketched in figure 7(*b*), which is a much-simplified representation, omitting some of the thin streamwise connecting vortices that are visible in figure 7(*a*). Although some of the sketched connections are only partially visible in the still frame, and the relative positions of some patterns in the direction normal to the image are not evident, observations of the video records permit the sketch of completed connections, as well as the identification of which connections pass in front of others, thus partially describing the three-dimensionality of connections. All vortices have been identified by a letter-number combination, with the letters S and N indicating vortices in the S- and N-cells, respectively, and numbers indicating the sequence of a vortex in the shedding process. Odd and even numbers indicate whether a vortex was shed from one side of the cylinder or the other.

Vortices S4 and N2 were shed in-phase, and connected across the N–S cell boundary along an uninterrupted, nearly straight line. Vortex N2, having a larger strength than vortex S4, appeared to balance its excess circulation by forming a loop to connect with vortex N1, which was shed from the opposite side of the large cylinder. Although shed nearly out-of-phase with both contemporary S-cell vortices S1 and S3, vortex N1 was also connected across the cell boundary, mainly to vortex S1. A rough balance

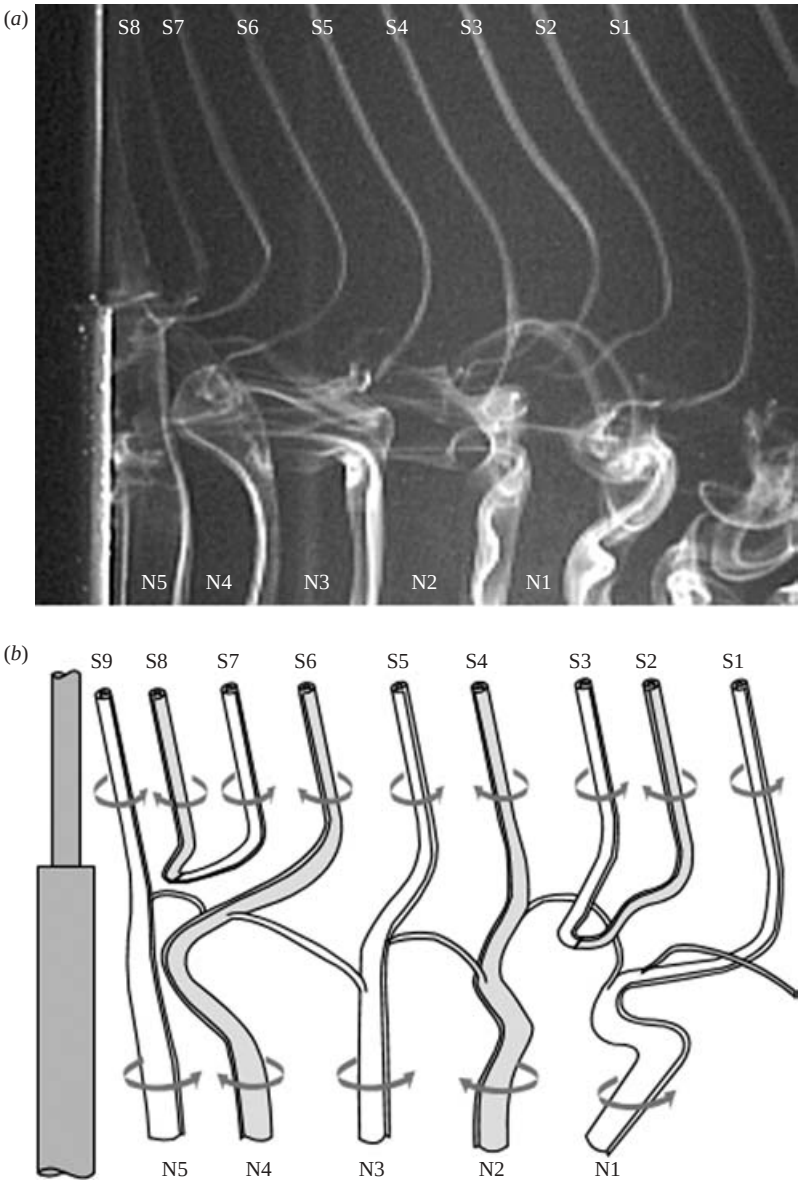

FIGURE 7. Connections between vortices in different cells at $Re_D = 152$. The large cylinder is located at negative values of y/D; (*a*) visualization image, (*b*) a sketch based on analysis of the video record, and which shows some details that may not be clearly visible in the still frames.

indicates that each of the two N-cell vortices N1 and N2 contributed about half of their strengths to their mutual connection, while the remaining halves went to connections with counterparts in the S-cell, S1 and S4, respectively. Two intermediate counter-rotating vortices in the S-cell, S2 and S3, remained unconnected to N-cell counterparts, but instead connected to each other through a half-loop. Similar looping processes have been observed by previous authors (e.g. Lewis & Gharib 1992) and may also be seen in figure 19 of Williamson (1992).

As vortices on either side of the N–S cell boundary were shed increasingly out-of-phase, their connections became increasingly distorted. Following the nearly-in-phase pair S4–N2, was pair S5–N3, which was somewhat out-of-phase and shows an inclined cross-boundary connection. The connection of the subsequent pair S6–N4 was even more inclined, resembling the connection between pair S1–N1, and tending further toward the streamwise direction. Vortex S7 was shed completely out-of-phase from either N3 or N5, and its end near the step was oriented almost completely in the streamwise direction. Instead of connecting mainly across the cell boundary, vortex S7 connected to the forthcoming counter-rotating vortex S8 in the same cell, thus repeating a process that occurred earlier with the S2–S3 pair. The subsequent vortex S9 was shed nearly in-phase with N5 and connected to it across the cell boundary, repeating the S4–N2 connection pattern.

In summary, all N-cell vortices were connected to both S-cell counterparts and N-cell counter-rotating mates, appearing to preserve their total strengths across all connections. In contrast, some S-cell vortices connected mainly across the cell boundary, while others connected mainly with counter-rotating mates in the same cell. In a cyclic process, two or three S-cell vortices connected across the boundary, followed by two vortices that connected to each other. This process is compatible with the ratio of shedding frequencies in the two cells, which was 0.53.

3.5.3. *Vortex connections at the N–L cell boundary*

Figure 8 shows one cycle in the development of the N-cell at $Re_D = 152$. The vortex-shedding frequencies in the N- and L-cells, calculated approximately from the video sequence from which the images in figure 8 were taken, were $f_N = 0.53$ Hz and $f_L = 0.63$ Hz, respectively, giving a frequency ratio of about 1.2. The sequence of vortex connections at the N–L cell boundary displayed qualitative similarities with the process discussed in the previous section, although it differed in detail because the differences between the frequencies and strengths of vortices in the L- and N-cells were much smaller than those in the N- and S-cells. Unlike the previous case, the majority of L-cell vortices would be expected to have counterparts in the N-cell. The given frequency ratio can be roughly achieved if six out of every seven vortex pairs have counterparts ($7/6 \approx 0.63/0.53 \approx 1.2$). Indeed, this is the case in the sequence shown in figure 8, in which vortices L13 and L14 do not have counterparts in the N-cell. Each cycle can be said to begin with an L-cell vortex pair that does not have a counterpart in the N-cell, which occurs after every seventh L-vortex pair is shed, or approximately 0.09 Hz (at 0.63 Hz, seven vortex pairs are shed in 11.1 s). This is very close to the beat frequency, $f_L - f_N = 0.10$ Hz (see also Lewis & Gharib 1992).

During part of the cycle, vortices in the N- and L-cells were shed in phase, and the two cells appeared to merge, with no evidence of a boundary between them. At some instance, a distinct N-cell started forming as a disturbance near the step. This stage is illustrated in figure 8(*a*) by vortex N1, which had a very short span and was highly curved toward the upstream direction at both its ends. Successive N-cell vortices had wider spans, and connected with vortices of the same sense of rotation in the L-cell (figure 8*b*, *c*). Streamwise filaments from each of the N-cell vortices trailed back toward the cylinder near each of the cell boundaries. As at the N-S cell boundary, the streamwise filaments formed looped connections with subsequent counter-rotating vortices in the same cell, although such filaments did not exist at the time of shedding. For example, the vortex pairs N3–L3 in figure 8(*a*) and N8–L8 in figure 8(*b*) are continuous, yet, at a later time, shown in figure 8(*c*), streamwise filaments are clearly visible at the cell boundary near both pairs.

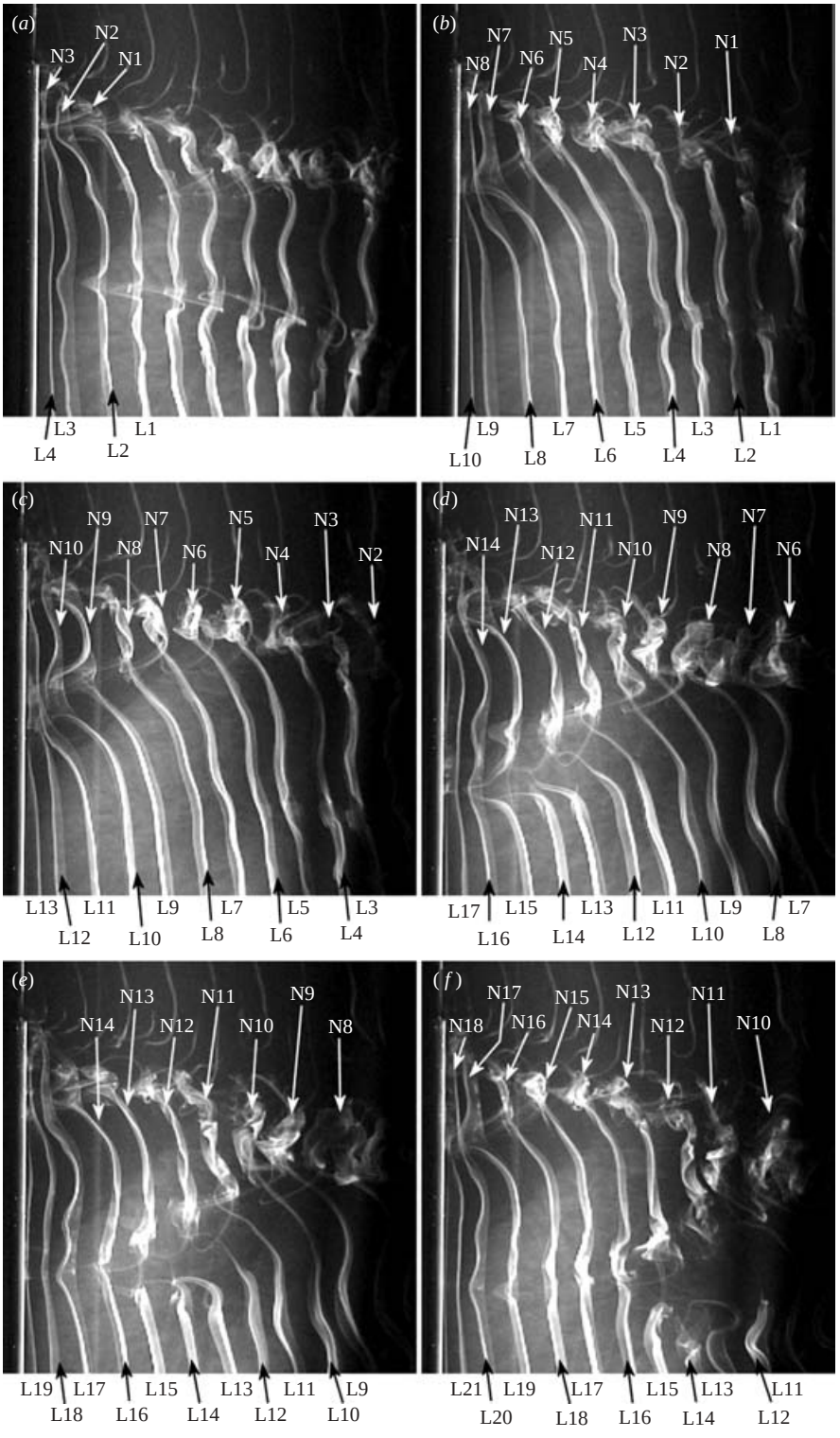

FIGURE 8. The near-step cell at $Re_D = 152$, visualized using the electrolytic precipitation method. The relative times of the images were (*a*) 0 s, (*b*) 5.07 s, (*c*) 7.71 s, (*d*) 11.55 s, (*e*) 12.78 s and (*f*) 15.05 s.

Linkages between vortices across the N–L cell boundary became progressively more inclined as a result of increasing spacing between corresponding vortices in the N- and L-cells, owing to the difference in their shedding frequencies. This is illustrated in figure 8(*d*) by the increased streamwise spacing between vortices N12 and L12, compared to that between the previously shed N11 and L11. The sequential cross-boundary pairing of vortices is interrupted when vortex N13 becomes connected to L15, rather than L13 (figure 8*d*), leaving vortices L13 and L14 without counterparts in the N-cell. As the flow moved downstream, the end of L13 bent toward vortex L14 (figure 8*e*), connecting the two vortices in a half-loop. Thin streamwise filaments also appeared to connect vortices L13 and L14 to L12 and L15, respectively. The half-loops did not form during shedding, but developed gradually and created visible links only at some downstream distance. Vortex N13 in figure 8(*d–f*), like N1 in figure 8(*a*), marks the beginning of a new N-cell cycle. Vortices N14 to N17 in figure 8(*f*) clearly show that the early vortices in the new N-cell were much reduced in span compared to the last few vortices of the previous cycle.

Each new N-cell resembled the previous one as it moved downstream, continuously growing in the spanwise direction, as the streamwise spacing between N- and L-cell vortices also grew. Each N-cell vortex was connected with an L-cell vortex rotating in the same sense, while thin streamwise filaments also connected subsequent N-cell vortices. Consecutive N-cells were separated by a pair of interconnected L-cell vortices. The number of vortex pairs associated with each N-cell varied.

3.6. *Wavelet analysis*

3.6.1. *Wavelet maps near the N–S cell boundary*

The velocity signal and wavelet map near the N–S cell boundary, at $y/D = -0.3$, are shown in figure 9 ($Re_D = 304$). The velocity signal (figure 9*a*) had an oscillation amplitude of about 15 % of the mean, which was much lower than that of a typical signal away from the cell boundaries. The amplitudes of the spectral peaks at this location (see figure 9*b*) were also much lower compared to those at other spanwise locations. A possible explanation of this observation is that the streamwise velocity component, which was the measured parameter, was relatively weak at this location, in which vortex dislocations formed quite frequently, generating vortex connections and streamwise loops at oblique orientations to the cylinder axis.

The velocity signal was frequency and amplitude modulated in the time-frame shown. During time intervals in which the signal exhibited a large modulation amplitude, for example in the ranges $27\text{ s} < t < 30\text{ s}$ and $41\text{ s} < t < 45\text{ s}$, the wavelet map (figure 9*b*) generally showed simultaneous peaks of comparable amplitudes at two dominant frequencies, $St = 0.390$ and $St = 0.198$. The lowest modulation amplitude of the signal occurred during time intervals in which the wavelet transform amplitude was lower than 40 % of the maximum, for example in the ranges $12\text{ s} < t < 15\text{ s}$, and $35\text{ s} < t < 37\text{ s}$. Williamson (1989) showed that vortex dislocations occurred when the signal modulation amplitude was minimum, and the present flow visualization has shown that vortex dislocations occurred when the vortices from different cells were shed out-of-phase (as with vortices N1 and S2–S3 in figure 7). It may then be inferred that strong modulation amplitude indicates time intervals in which vortices in the two cells are shed in-phase and connected to each other across the cell boundary. It must be emphasized, however, that not all such events are captured in the wavelet map, because the LDV measurement volume, which was positioned at a fixed spanwise location, would at times be within the S-cell, at the N–S cell boundary, or within the N-cell, depending on the relative location of the inclined boundary between the

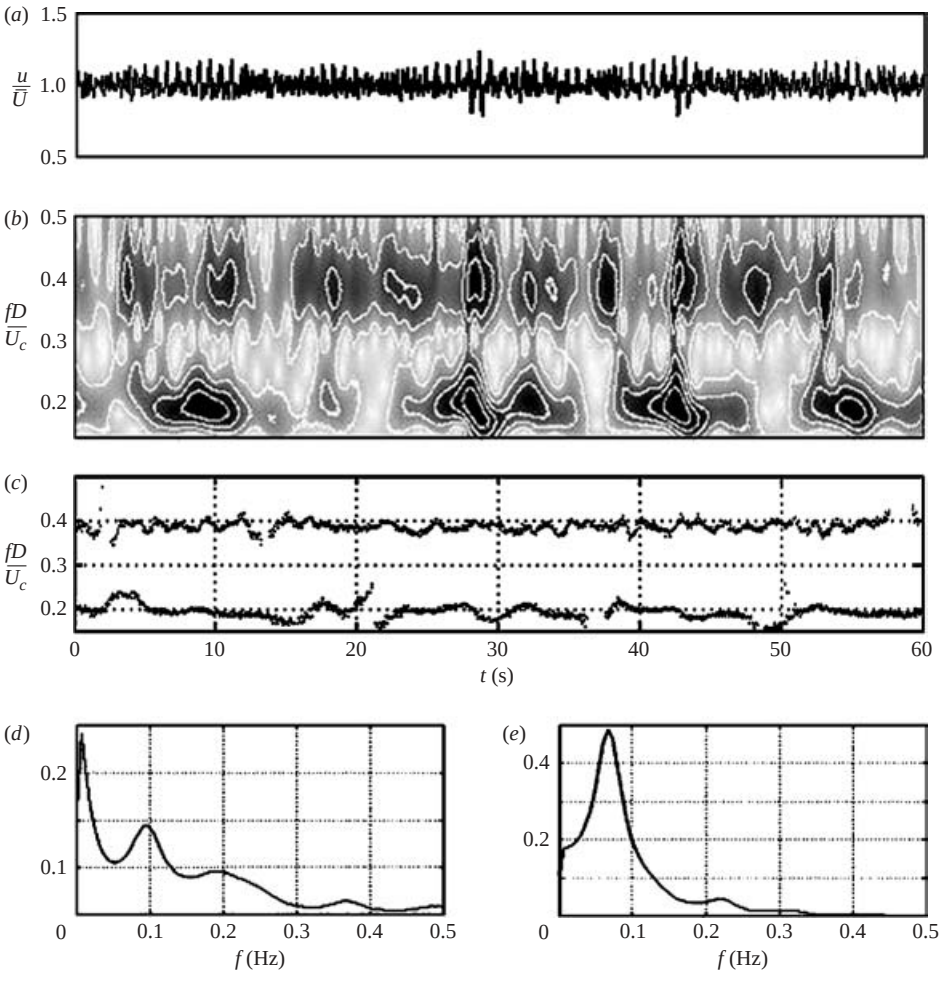

FIGURE 9. (*a*) Velocity signal, (*b*) wavelet map, and (*c*) peak local frequencies at $y/D = -0.3$, $Re_D = 304$. Smooth spectra, estimated from 205 s long records, are also provided for the wavelet signals at (*d*) $St = 0.390$ and (*e*) 0.198.

two cells. Given that the vortex-shedding frequency ratio was $f_N/f_S = 0.508$, and that $f_S = 2.72$ Hz, the average spacing between dislocations can be estimated as 0.75 s. The inverse of this value, 1.3 Hz, essentially matches the beat frequency $f_S - f_N$, but is much higher than the local modulation frequency of 0.09 Hz, estimated roughly as the peak frequency of the spectrum of the wavelet signal at the dominant frequency within the S-cell ($St = 0.390$; figure 9*d*). This modulation frequency, which was approximately equal to the beat frequency between the N- and L-cells, is a characteristic of the N-cell (Lewis & Gharib 1992). Wavelet analysis of velocity signals in the S-cell away from the step (not presented here) showed no signs of modulation.

As shown in the previous section, the collapse of the N-cell was related to vortex dislocations at the N-L cell boundary. At $Re = 304$, the shedding ratio at this boundary was $f_N/f_L = 0.947$, which means that dislocations were separated by approximately 19 L-cell vortex pairs or 18 N-cell pairs. At a shedding rate of $f_N = 1.38$ Hz, the N-cell cycle should recur every 13 s, which matches the inverse of the beat frequency between the N- and L-cells, $1/(f_L - f_N)$. A spectrum of the wavelet signal at $St = 0.198$, in the

N-cell (figure 9*e*), shows a modulation frequency of 0.07 Hz, which is not too far from the beat frequency $f_L - f_N = 0.08$ Hz. Lewis & Gharib (1992) also observed modulation in the N-cell at the beat frequency. The amplitude of the wavelet spectral peak at the N-cell dominant frequency (figure 9*e*) was significantly higher than that at the S-cell dominant frequency (figure 9*d*), which is additional evidence that modulation is an N-cell and not S-cell characteristic. The simultaneous appearance of high amplitudes at both dominant frequencies in the wavelet map indicates that the measurement volume would probably be occupied by a cross-boundary vortex connection. Similarly, a lack of peaks in the wavelet map would indicate that the measurement volume would be in a region in which S-cell vortices connect to each other rather than to N-cell vortices. An example can be seen by the region below the half-loop connection between vortices S2 and S3 in figure 7. When the measurement volume was located in the interior of either the S-cell or the N-cell, amplitude peaks would appear in the wavelet map at only one local frequency. This is the case in the ranges $6\,\mathrm{s} < t < 9\,\mathrm{s}$ (peak at the low frequency) and $15\,\mathrm{s} < t < 25\,\mathrm{s}$ (peak at the high frequency). The large gap at low frequency in the range $12.5\,\mathrm{s} < t < 25\,\mathrm{s}$, followed by two low-frequency peaks in quick succession, is probably because the N-cell cycle was not completely regular, as the number of vortex pairs would vary from one cycle to the next.

The variation of Strouhal numbers at which amplitude peaks were observed in the wavelet map are plotted against time in figure 9(*c*). Both local peak frequencies fluctuated slightly in a non-systematic manner about their means, with the lower frequency fluctuating at a slower rate. As with the spreading of the spectral peaks, these fluctuations are attributed to slow changes in the vortex inclinations.

3.6.2. *Wavelet maps near the N–L cell boundary*

The velocity signal and wavelet map at $y/D = -6.4$, near the N–L cell boundary, are shown in figure 10.

The velocity signal had a maximum oscillation amplitude of approximately 50 % of the mean, which was much larger than that at the N–S cell boundary, and it was clearly modulated (figure 10*a*). During time intervals in which the signal exhibited large modulation amplitude, the wavelet map (figure 10*b*) generally showed large amplitude within a relatively wide frequency band. The Fourier spectrum at this location (see figure 6*e*) showed peaks at the dominant frequencies in both N- and L-cells, at $St = 0.198$ and 0.209, respectively, and wide non-zero bands at the base of each peak. In the ranges centred around 25 s, 35 s and 50 s, the highest contour encircled both of these dominant frequencies. Minimum modulation amplitude of the signal occurred during time intervals in which the wavelet transform amplitude was much closer to the background level, for example, at 12 s, 38 s and 55 s.

As previously mentioned, the N–L cell boundary was inclined to the streamwise direction, at a larger angle, and in the opposite sense, to the N–S cell boundary. Viewed from the fixed location of the LDV measurement volume, the N–L cell boundary would appear to shift spanwise with time, in a direction away from the step. Thus, the LDV signal would first record the passage of L-cell vortices at the higher frequency, followed by patterns near the cell boundary that might include streamwise loops between successive N-cell vortices, N–L vortex connections, and possibly vortex dislocations, and finally the passage of N-cell vortices at the lower frequency, before abruptly restarting the cycle. The N-cell frequency can be observed around $t = 9$ s and 15 s, while the L-cell frequency can be observed around $t = 3$ s and 57 s. Durations without any peaks might be caused by long intervals of highly inclined vortex connections or dislocations. The beat frequency of the two cells,

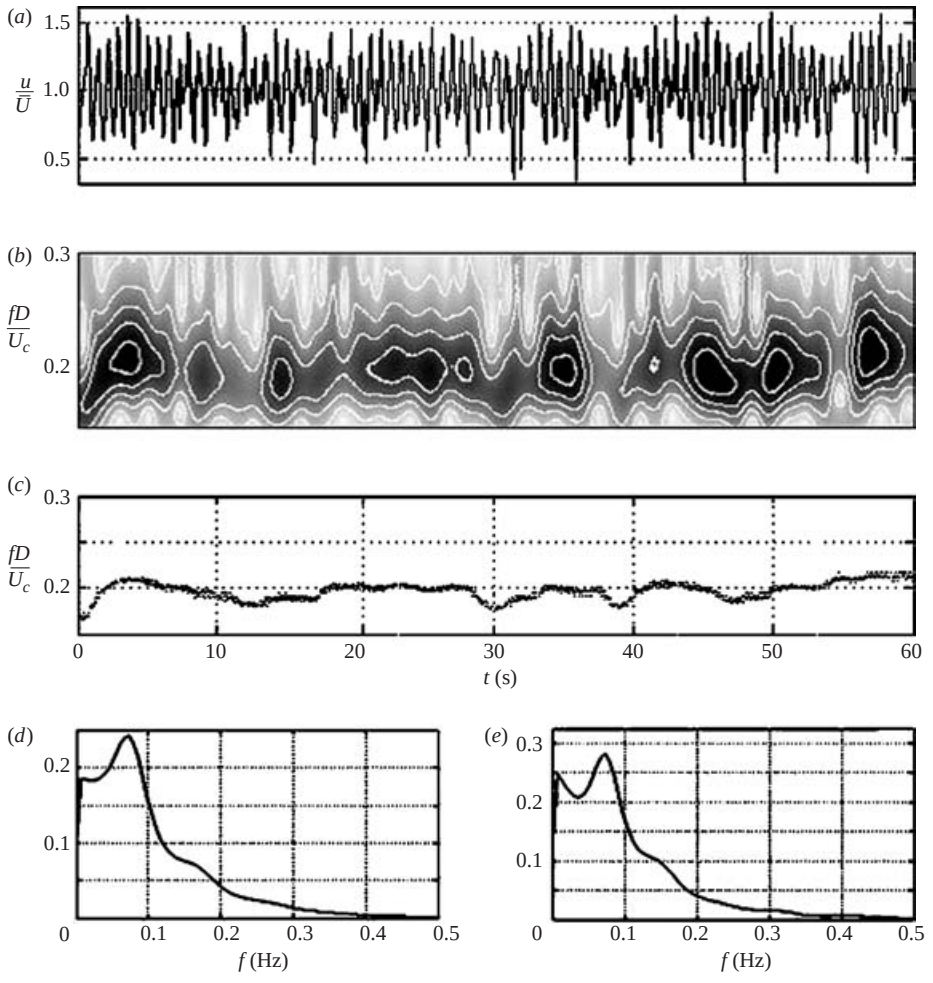

FIGURE 10. (*a*) Velocity signal, (*b*) wavelet map, and (*c*) peak local frequencies at $y/D = -6.4$, $Re_D = 304$. Smooth spectra, estimated from 205 s long records, are also provided from the wavelet signals at (*d*) $St = 0.198$ and (*e*) 0.210.

$f_L - f_N = 0.08$ Hz, is approximately equal to the modulation frequency of 0.07 Hz estimated from the spectral peaks of the wavelet signals at the dominant frequencies in both the N- and L-cells (figures 10*d* and 10*e*, respectively).

The values of the local peak frequencies fluctuated in time (figure 10*c*), with an amplitude comparable to that at the N–S cell boundary, and a period that was comparable to that in the N-cell. As previously, this fluctuation can be attributed to the changing inclination of the vortices with time. It appears that the LDV measurement volume was situated within the L-cell (and the boundary) longer than it was within the N-cell, as the local frequency peaked for long durations around $St = 0.209$ (or below the cutoff threshold), and less frequently around the mean N-cell frequency, at $St = 0.198$.

3.7. *Streamwise vortices*

As the upstream fluid approached the step-cylinder in the region near the step, the streamlines on the symmetry plane tended to deflect spanwise toward the small

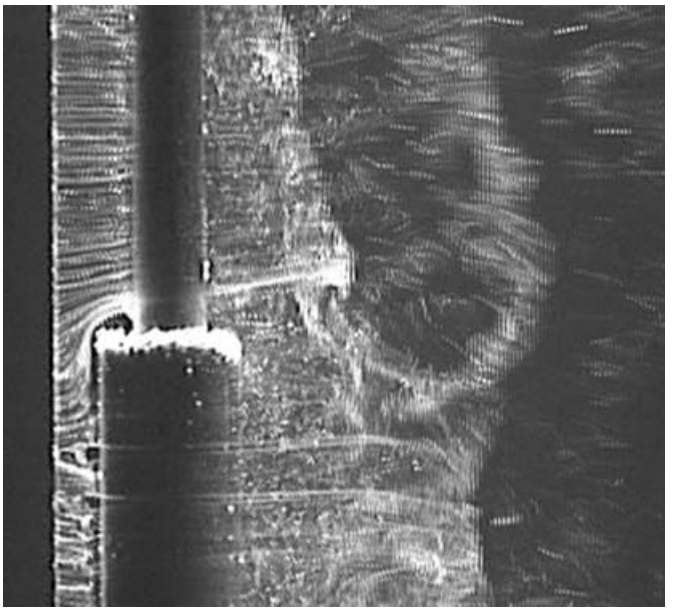

FIGURE 11. Separation over the leading edge of the step, visualized using hydrogen bubbles at $Re_D = 1230$.

cylinder, separating from the leading edge of the step and forming a recirculation bubble at the root of the small cylinder, as shown in figure 11. The recirculating fluid formed a 'junction vortex', the two branches of which became wrapped around the small cylinder and became oriented with their axes roughly into the streamwise direction, as depicted in figure 2. When viewed from downstream, the left-hand vortex branch turned clockwise and the right-hand vortex branch turned counterclockwise. Blockage by the small cylinder and induced rotation by the junction vortex diverted the forthcoming fluid sideways, causing it to spill over the edges of the step toward the low-pressure regions on the sides of the large cylinder, where it rolled up into two streamwise 'edge vortices'. These vortices were counter-rotating to the adjacent branches of the junction vortex; when viewed from downstream, the left-hand edge vortex turned counterclockwise, while the right-hand edge vortex turned clockwise. The existence of vortices originating at the step was speculated by Ko *et al.* (1983), who referred to them as 'leading-edge type vortices', presumably in reference to vortices generated by delta wings.

While the edge vortex could be clearly seen close to the cylinder in nearly all visualizations, the junction vortex was observed only under carefully controlled conditions. As this was not a main focus of the study, only limited attempts were made to visualize the junction vortex. Toward this end, a much larger step-cylinder was used, with diameters $D = 50$ mm and $d = 25$ mm, and a Reynolds number of $Re_D \approx 1100$ (the lowest achievable with this cylinder for stable flow within the present water channel), and a hydrogen-bubble wire was placed in contact with the step upstream of the junction between the two cylinders. Samples of the best still images show the junction and edge vortices together in figure 12. The two images were taken at different times and do not represent a sequence. Sketches of the relevant patterns are presented next to each still image to identify the streamwise vortices among irrelevant patterns, such as disturbances produced by the hydrogen bubble wire supports.

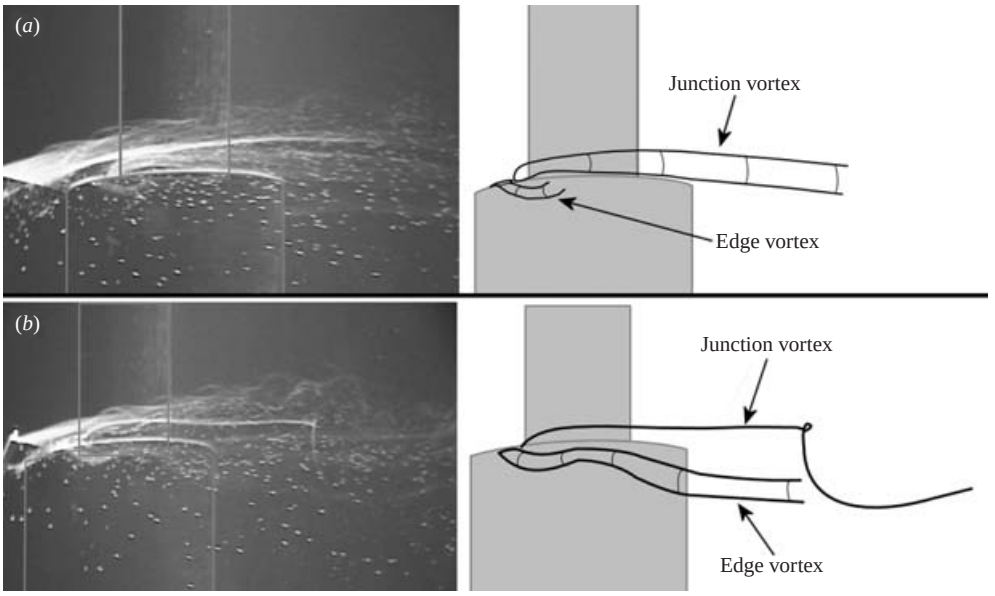

FIGURE 12. The junction and edge vortices, at $Re_D = 1100$.

The edge vortices rolled-up over the sides of the large cylinder at nearly right angles with respect to the symmetry plane, and not near the leading edge of the step as figure 12(*a*) seems to indicate (the viewing perspective in this figure was from the back and side). Both vortices attained nearly streamwise orientations shortly after forming, and remained roughly horizontal until they began to interact with the S-cell vortices.

About one diameter downstream of the cylinder axis, the junction vortex became entangled in the velocity field induced by S-cell vortices (figure 12*b*), and disappeared from view. Because the junction vortices and the S-cell vortices could not be visualized well together, their interactions could not be documented in detail and no specific conclusions can be made with the available information. The edge vortices were not visible very far downstream under these conditions, but, as shown in figure 13, they were also heavily entrained in the S-cell vortices. As the edge and junction vortices were completely dominated by the rotation of the S-cell vortices, it seems reasonable to conclude that the streamwise vortices were much weaker than the spanwise vortices.

3.8. *Streamwise vortex connections*

As seen in figure 7, the S-cell vortices reversed their inclination with respect to the cylinder axis and became nearly streamwise, while stretching upstream toward the step. Figure 13 indicates that the streamwise parts of these vortices are visible through precipitation that originated in the edge vortices, and possibly also in the junction vortices. When an N-cell counterpart to an S-cell vortex was shed, the cross-boundary connection overwhelmed any connection with edge and/or junction vortices.

The detailed process of edge-vortex interactions with S-cell vortices at $Re_D = 118$ is illustrated in the image sequence and sketches in figure 13. The sketches were based on extensive study of the video record, and include connections that may not be easily identified in the still images, including evidence of which connections passed in front of others, allowing some three-dimensional information to be imparted in a two-dimensional drawing. The initial stage of interaction is the entanglement of

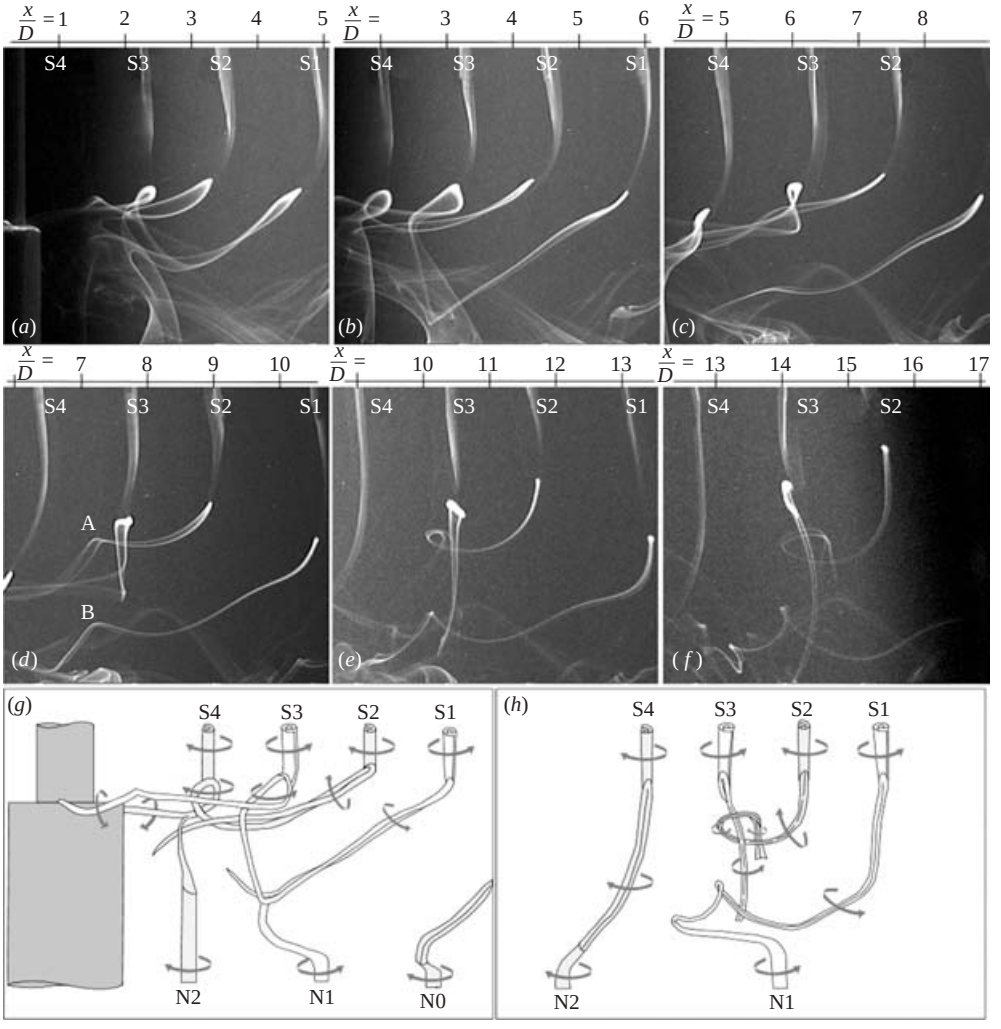

FIGURE 13. Vortex half-loop formation, visualized using electrolytic precipitation at $Re_D = 118$. The relative times of the images were (*a*) 0 s, (*b*) 1.94 s, (*c*) 4.84 s, (*d*) 7.81 s, (*e*) 12.45 s and (*f*) 18.49 s. Sketches (*g*) and (*h*) correspond to images (*b*) and (*f*), respectively. Sketches are based on analysis of the video record, and show details that may not be clearly visible in the still frames.

an edge vortex by a newly shed S-cell vortex, as seen in figure 13(*a*), in which an edge vortex is entangled by vortex S4. Further downstream, the edge vortex is twisted around the axis of an S-cell vortex from the same side of the cylinder, forming a loop between two branches that connect the edge vortex with two adjacent S-cell vortices, also shed from the same side of the cylinder. In figure 13(*a*), this is shown by an edge vortex being twisted by S3 to form a loop connecting it with S1 and the forthcoming S5. As the edge vortex becomes more twisted, its two branches are drawn toward each other, become intertwined and become part of an S-cell vortex (see vortex S1, for example), at which stage, the edge vortex is very unlikely to retain any of its initial strength. Note that the entrainment of an edge vortex to two consecutive S-cell vortices from the same side of the cylinder, as described above, leads to opposing

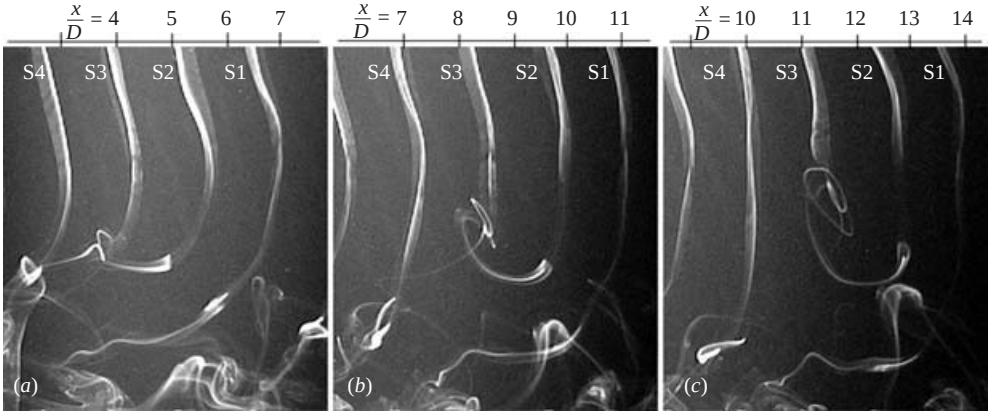

FIGURE 14. Vortex half-loop formation, visualized using electrolytic precipitation at $Re_D = 168$. The relative times were (*a*) 0 s, (*b*) 3.37 s and (*c*) 5.91 s.

directions of rotation of the two sides of each branch. This cannot be sustained, and the branch will eventually snap.

Once 'snapped', each side of the edge vortex became integrated into either a half-loop connection between two S-cell vortices shed from opposite sides of the cylinder, or to a cross-boundary connection with an N-cell vortex, as seen in the images in figures 13(*b*) to 13(*f*) and the sketches in figures 13(*g*) and 13(*h*). As vortices S1 and S3 were convected downstream, their connection (figures 13(*b*) and 13*g*) was stretched spanwise toward the large cylinder. A similar connection can be seen in the hydrogen bubble photograph in figure 5(*b*). After this connection snapped (figure 13*c*), the side toward S1 became connected to N1, while the side toward S3 eventually connected to S2 (note that neither S2 nor S3 had counterparts in the N-cell). At the same time, the connection between vortices S2 and S4 snapped as well. Its side towards S2 was twisted by vortex S3 around itself until the two vortices became perceptibly connected further downstream (figure 13*e–f*, *h*).

The final stage of the half-loop connection between two counter-rotating S-cell vortices is shown in figure 14. As in the previous sequence, vortex S2 looped around vortex S3 and formed a helical pattern. The video sequence showed that the connection of vortices S3 and S5 dissipated to become invisible at some downstream distance.

3.9. *Single-sided vortex shedding*

In order to examine vortices entirely free of cross-boundary connections, some experiments were performed in the range of Reynolds numbers in which only the large cylinder shed vortices. As with previous figures where sketches were included, the sketches in figure 15 were based on extensive study of the video record, which allowed connections to be sketched where they may appear vague in the still images, and also showed which connections passed in front of others, allowing some three-dimensional information to be imparted in a two-dimensional drawing. At $Re_D = 63$, corresponding to $Re_d = 32$ (figure 15*a*), there were no S-cell vortices, and vortices in the N-cell did not appear to form fully. Moreover, L-cell vortices were well defined only at about $4D$ spanwise distances from the step. Close to the step, edge vortices can be seen, but they disappeared further downstream, probably disintegrating under the influence of L-cell vortices.

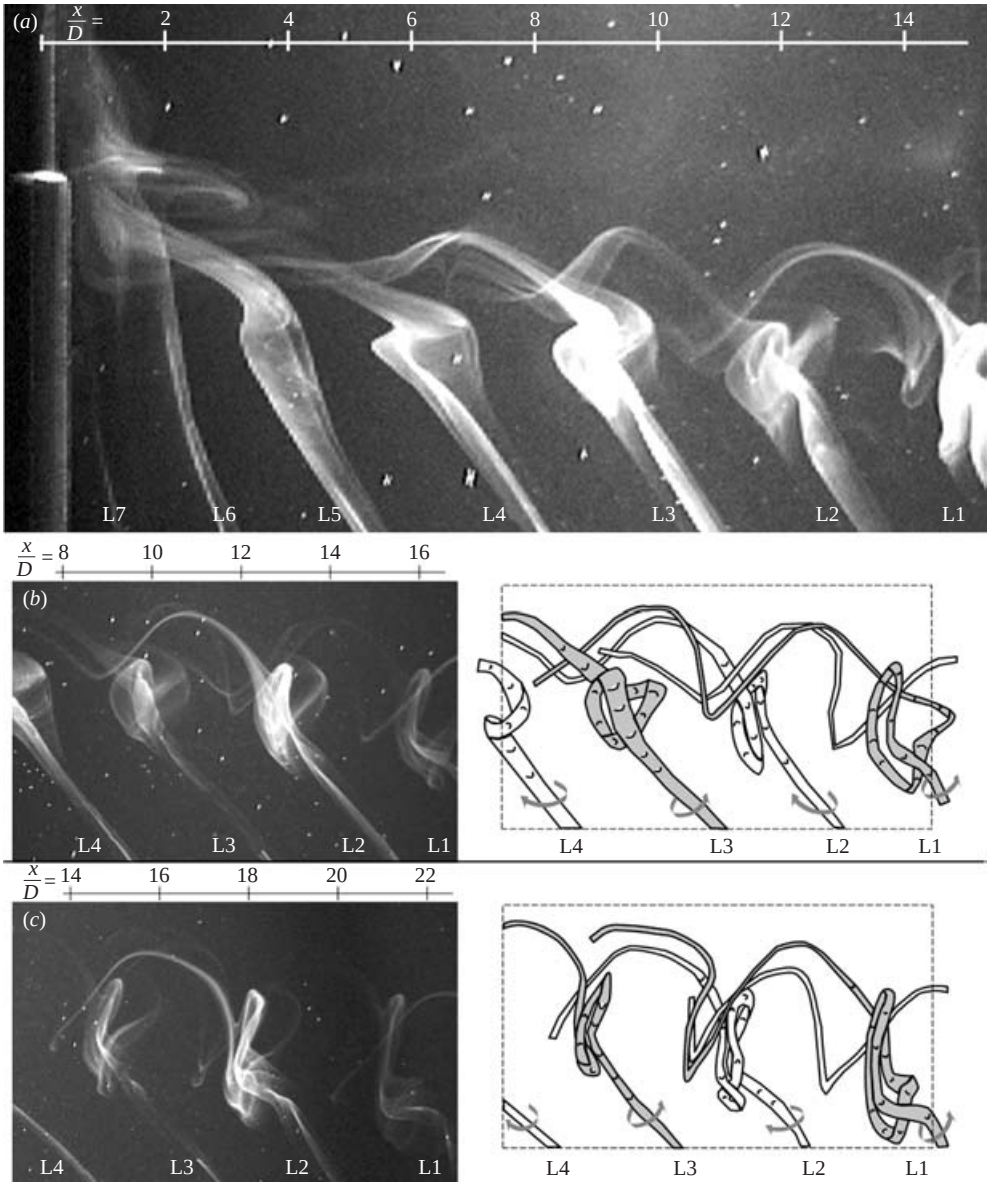

FIGURE 15. Vortex shedding from the large cylinder only, visualized using the electrolytic precipitation method. $Re_D = 63$, $Re_d = 33$. There is a 4.14 s delay between (*b*) and (*c*). Sketches are based on analysis of the video record, and show details that may not be clearly visible in the still frames.

In the step region, the inclination of the L-cell vortices changed abruptly (figure 15*a*), as they stretched upstream toward the cylinder, and became further inclined into the streamwise direction with downstream distance. The inclined and main parts of the vortices became distorted under the influence of each other's induced velocity fields. Subsequent L-cell vortices were twisted laterally into helical loops (figure 15*b*), which grew more complex with downstream distance (figure 15*c*). The inclined parts of the vortices were stretched into a wavy pattern, with the maximum deflection of the wave

occurring close to each of the shed vortices. Persistent twisting of the inclined parts eventually generated half-loop connections between vortices shed from opposite sides of the cylinder, as between L2 and L3 in figure 15(*c*). The wavy pattern and half-loop connections appear remarkably similar to those observed near the free tip of a finite cylinder (Zdravkovich 2003).

4. Conclusions

Complex vortex-shedding patterns and vortex interactions were examined in detail near cylinders with a sudden change in diameter. At spanwise distances far from the step, spectral peaks occurred at vortex-shedding frequencies close to the values for uniform cylinders at the same local Reynolds number. Near the step, however, a distinct cell of lower shedding frequency developed behind the large cylinder. This cell formed and disappeared in a recurring, though not periodic, manner. Local frequency analysis confirmed that the dominant frequency in the cell boundary regions varied with time.

Flow visualization showed that interactions between vortices at cell boundaries took several forms. Vortices in the N-cell could connect with counterparts across the cell boundaries, while half-loop connections also formed between vortices shed from opposite sides of the cylinder within the N-cell. Owing to the difference in shedding frequency between cells, vortices were shed increasingly out-of-phase across the cell boundaries, creating large inclinations in the connections. When vortices in the S- or L-cells were shed without counterparts in the N-cell, half-loops would connect vortices of opposite sign. Streamwise edge and junction vortices rolled up at the sharp side edges of the step and were observed to interact with the S-cell vortices. The visualizing material contained within the edge vortices became integrated into the S-cell vortices, allowing a detailed examination the formation of a half-loop connection. When vortices were shed from the large cylinder only, the L-cell vortices bent back toward the cylinder, and caused helical twisting and half-loop connections between subsequent vortices shed from opposite sides of the cylinder.

The formation of the N-cell near the step has been plausibly associated with downwash from the trailing edge of the step and the resulting recirculation which decreases the shedding frequency compared to parts away from the step.

This work has been supported by the Natural Sciences and Engineering Research Council of Canada.

REFERENCES

Abry, P. 1997 *Ondelettes et Turbulences: Multirésolutions, Algorithmes de Décomposition, Invarience d'Échelle et Signaux de Pression*. Diderot Multimedia, Paris.

Adrian, R. J. & Yao, C. S. 1987 Power spectra of fluid velocities measured by laser Doppler velocimetry. *Exps. Fluids* **5**, 17–28.

Ayoub, A. & Karamcheti, K. 1982 An experiment on the flow past a finite circular cylinder at high subcritical and supercritical Reynolds numbers. *J. Fluid Mech.* **118**, 1–26.

Bénard, H. 1908 Formation de centres de giration à l'arrière d'un obstacle en mouvement. *C. R. Acad. Sci. Paris* **147**, 839–842.

Berger, E. & Wille, R. 1972 Periodic flow phenomena. *Annu. Rev. Fluid Mech.* **4**, 313–340.

Chua, L. P., Liu, C. Y. & Chan, W. K. 1998 Measurements of a step cylinder. *Intl Commun Heat Mass Transfer* **25**, 205–215.

Daubechies, I. 1992 Ten lectures on wavelets. *CBMS-NSF Regional Conference Series in Applied Mathematics*, SIAM, Philadelphia.

Farge, M. 1992 Wavelet transforms and their applications to turbulence. *Annu. Rev. Fluid Mech.* **24**, 395–457.

Gaster, M. 1969 Vortex shedding from slender cones at low Reynolds numbers. *J. Fluid Mech.* **38**, 565–576.

Gordeyev, S. V. & Thomas, F. O. 1999 Temporal subharmonic amplitude and phase behaviour in a jet shear layer: wavelet analysis and Hamiltonian formulation. *J. Fluid Mech.* **394**, 205–240.

Jordan, D., Miksad, R. W. & Powers, E. J. 1997 Implementation of the continuous wavelet transform for digital time series analysis. *Rev. Sci. Instrum.* **68**, 1484–1494.

von Kármán, T. 1911 Über den Mechanismus des Widerstandes den ein bewegter Körper in einer Flüssigkeit erzeugt. *Nachr. Ges. Wiss. Göttingen, Math. Phys. Klasse* Part 1: 509–515, Part 2: 547–556.

Ko, N. W. M. & Chan, A. S. K. 1984 Pressure distributions on circular cylinders with stepwise change of the diameter. *ASME Paper* 84-WA/FE-13.

Ko, N. W. M., Chan, A. S. K. & Kan, S. M. 1983 Flow behind stepped and tapered coaxial cylinders. *Proc. 2nd Asian Congr. Fluid Mech. Beijing, China*, pp. 755–760.

Ko, N. W. M., Leung, W. L. & Au, H. 1982 Flow behind two coaxial circular cylinders. *Trans. ASME* I: *J. Fluids Engng* **104**, 223–227.

Lewis, C. G. & Gharib, M. 1992 An exploration of the wake three dimensionalities caused by a local discontinuity in cylinder diameter. *Phys. Fluids* A **4**, 104–117.

Mair, W. A. & Stansby, P. K. 1975 Vortex wakes of bluff cylinders in shear flow. *J. Appl. Maths* **28**, 519–540.

Norberg, C. 1992 An experimental study of the flow around cylinders joined with a step in diameter. *11th Australasian Fluid Mech. Conf.*, pp. 507–510.

Papangelou, A. 1992 Vortex shedding from slender cones at low Reynolds numbers. *J. Fluid Mech.* **242**, 299–321.

Taneda, S., Honji, H. & Tatsuno, M. 1979 The electrolytic precipitation method of flow visualization. In *Flow Visualization: Proceedings of the International Symposium on Flow Visualization (ed. T. Asanuma), 1977, Tokyo, Japan*, pp. 209–214.

Torrence, C. & Compo, G. P. 1998 A practical guide to wavelet analysis. *Bull. Am. Met. Soc.* **79**, 61–78.

Valles, B., Andersson, H. I. & Jenssen, C. B. 2002 Direct-mode interactions in the wake behind a stepped cylinder. *Phys. Fluids* **14**, 1548–1551.

Van Dyke, M. 1982 *An Album of Fluid Motion.* Parabolic, Stanford, California.

Williamson, C. H. K. 1989 Oblique and parallel modes of vortex shedding in the wake of a circular cylinder at low Reynolds numbers. *J. Fluid Mech.* **206**, 579–627.

Williamson, C. H. K. 1992 The natural and forced formation of spot-like 'vortex dislocations' in the transition of a wake. *J. Fluid Mech.* **243**, 393–441.

Williamson, C. H. K. 1996 Vortex dynamics in the cylinder wake. *Annu. Rev. Fluid Mech.* **28**, 477–539.

Yagita, M., Kojima, Y. & Matsuzaki, K. 1984 On vortex shedding from circular cylinder with step. *Bull. JSME* **27**, 426–431.

Zdravkovich, M. M. 1997 *Flow Around Circular Cylinders, Vol. 1: Fundamentals.* Oxford University Press.

Zdravkovich, M. M. 2003 *Flow Around Circular Cylinders, Vol 2: Applications.* Oxford University Press.

Zdravkovich, M. M., Brand, V. P., Mathew, G. & Weston, A. 1989 Flow past short circular cylinders with two free ends. *J. Fluid Mech.* **203**, 557–575.